

magmatic segments, show creep and some stick-slip behavior (with cumulative LOS displacement up to ~30-40 mm over a ~5 years period) accompanied by low-level seismicity. Some of the creeping faults are also spatially associated with hydrothermal springs. We interpret that the temporal behavior of the faults in the linkage zone is controlled by the interplay between tectonic extension, high heat flows and fluid circulation near the magmatic segments where creeping of some faults is favored.

Plain Language Summary

The exterior of the Earth is teared apart along mid-ocean ridges where magma rises and new oceanic crust is created. Mid-ocean ridges have an unmissable zig-zag pattern because while some portions, called ridge segments, are being teared apart others, called offsets, slide past each other. However, how the Earth deforms in these offsets is today poorly understood. The Afar region is the perfect place to address this open question as it is one of the few places where a mid-ocean ridge is emerged and the segment and offsets can be observed on-land.

In this study we combine satellite and earthquakes measurements to film how the surface of the Earth moves in an offset. We show that the network of fractures at the surface of an offset can move either with sudden motions generating major earthquakes or they can slip continuously over years and produce many smaller earthquakes. Our results provide one of the few direct observations of the different type of motion of the Earth in an offset of the mid-ocean ridge system.

1. Introduction

During continental rupture, the plate boundary zone is segmented along its length to form discrete rift segments which accommodate plate divergence through tectonic and magmatic activity (Hayward & Ebinger, 1996; Manighetti et al., 2001; Keir et al., 2009). As plate divergence proceed to continental break-up, adjacent rift segments grow and interact through linkage zones which may develop into oceanic transform faults (e.g. Taylor et al., 2009; Gerya, 2013; Leroy et al., 2012; Le Pourhiet et al., 2017). Therefore, linkage zones play a key role in shaping the future plate boundary. However, how deformation is distributed across a linkage zone and how much strain is accommodated by stick-slip faulting or by continuous creep is largely unknown. The complex fault patterns of linkage zones have prevented achieving a clear understanding of their kinematics. In recent years, deformation of different styles of oceanic transforms have also been measured in Iceland using geodesy, seismicity and structural geology (e.g. Brandsdóttir & Einarsson, 1979; Einarsson & This article has been accepted for publication and undergone full peer review but has not been through the copyediting, typesetting, pagination and proofreading process, which may lead to differences between this version and the [Version of Record](#). Please cite this article as doi: [10.1029/2020JB021387](#).

Brandsdóttir, 1979; Opheim & Gudmundsson, 1989 Einarsson, 2008; Decriem & Árnadóttir, 2012; Geirsson et al., 2012; Metzger et al., 2013; Metzger & Jónsson, 2014). However, little is known about active deformation in rift linkage zones of continental rifts with our knowledge is mainly based on theoretical models (e.g. Tapponier & Varet, 1974; Corti, 2012; Allken et al., 2012; Brune et al., 2017) and rare observations (e.g. Doubre et al., 2017a; Pagli et al., 2019; La Rosa et al. 2019). Today, the growing body of SAR acquisitions on exposed continental rift systems offers the perfect opportunity to investigate, at high spatial and temporal resolution, the kinematics of rift linkage zones.

In this study we combined InSAR time-series analysis and modeling with seismicity to probe the present-day kinematics of the Afrera Plain in Northern Afar (Ethiopia). Previous studies encompassing seismicity, numerical modeling, field observations and geodetic measurements suggested that the Afrera Plain is an active linkage zone between the Erta Ale and Tat Ali rift segments, but whether this linkage zone may evolve into a transform fault is still debated (Bonatti et al., 2017; Illsley-kemp et al. 2018; La Rosa et al., 2019). A recent study by La Rosa et al. (2019) used InSAR, seismicity and structural geology to investigate a fault slip in Afrera associated with a M_L 5.0 in 2007 and proposed a model of rift linkage consisting of a right-lateral, NW-SE-trending transfer zone where deformation is accommodated by dominant ~NS-striking faults with oblique kinematics characterized by both normal and left-lateral components (Figure 1). Here, we processed a large SAR dataset from ENVISAT and Sentinel-1 (S1) catalogues spanning the time periods 2005-2010 and 2014-2019 to produce time-series of cumulative displacements and the related uncertainties. We identified deformation along different faults with both stick-slip faulting, in January 2018 but also fault creep throughout the observation period. Modeling of both types of faults showed motion along ~NS-striking planes with oblique kinematics, similar to the 2007 event (La Rosa et al., 2019). We also investigated how seismicity accompany the observed deformation in space and time across the linkage zone. To this aim, we used the available catalogues 2005-2010 (Belachew et al. 2011; Illsley-Kemp et al., 2018; La Rosa et al., 2019) but also analyzed new data from two local seismic networks (Doubre et al., 2017b; Keir et al., 2017; La Rosa et al., 2021) to study the seismic sequence in January 2018 and we identified two major earthquakes with $M_L > 5$ (Figure 1a). This study presents one of the few direct observations of the fault kinematics in a rift-linkage also detailing the temporal evolution of the strain. Our results show that Afrera is a linkage zone where the overall right-lateral motion between Erta Ale and Tat Ali is taken up by NS-striking faults with dominant

left-lateral strike-slip and normal kinematics (Figure 1b). We document how creep and stick-slip are partitioned across the Afrera linkage zone and observe that creeping faults are located in proximity to the active magmatic segments and hydrothermal springs, suggesting that the creeping fault behavior could be controlled by high heat flows and hydrothermal fluids circulation.

2. Tectonic Setting

The Afar depression is the triple junction between the East African, Gulf of Aden and Red Sea rifts accommodating the separation of the Nubian, Somali and Arabian Plates during the last 30 Ma (Barberi & Varet, 1970; Manighetti et al., 1998; Beyene & Abdelsalam, 2005). Starting from ~11 Ma, the Red Sea rift stepped on land south of ~16°N, creating the Danakil Depression in Northern Afar (e.g. Eagles et al., 2002). Extension in Afar was initially accommodated by large-scale border faults which today bounds the Afar rift floor from the Ethiopian Plateau to the west. Since the Quaternary, extension migrated to a series of en-echelon magmatic rift segments where the majority of magmatic activity and faulting now occur (e.g. Hayward & Ebinger, 1996; Keir et al., 2009).

Recent GPS measurements show that, in Northern Afar, the ~N50°E-directed extension increases southeastward from ~6.7 mm/yr at ~N15° to ~16 mm/yr at ~N12° (Figure 1a) (Viltres et al., 2020). Two main magmatic segments accommodate extension in Northern Afar: The Erta Ale (EA) and Tat Ali (TA) segments (Figure 1). Here, the most recent magmatic episodes occurred on the volcanoes of the EA segment: a magma withdrawal and normal faulting event sometime during 1993 to 1996 at Gada Ale (Amelung et al., 2000), an intrusion in 2004 at Dallol (Nobile et al., 2012), an eruption in 2008 at Alu-Dalafilla (Pagli et al., 2012), and finally at Erta Ale an intrusion in 2004 (Barnie et al., 2016b), a small eruption in 2010 (Field et al., 2012), and a major eruption in 2017 (Xu et al., 2017; Moore et al., 2019).

The EA and TA segments strike ~N330°E and are arranged en-echelon, with the EA segment left-stepping with respect to TA (La Rosa et al., 2019). The two segments partially overlap within a ~20km-wide area known as Afrera Plain (AP) (Figure 1). The AP is a depressed region reaching ~100 m below sea level (b.s.l.) and hosting a salt water lake (Afrera Lake) fed by hydrothermal springs (Figure 1b) (Bonatti et al., 2017; Brinckmann & Kürsten, 1970). The AP is clearly bounded to the east by systems of west-dipping normal faults which are the northern-most tip of TA and also cut the eastern shore of the lake (Bonatti

et al., 2017). Conversely, the western termination of the AP, as it links to the EA segment, is not as well-defined. Evaporitic deposits and fresh basalts outcrop in the AP (Keir et al., 2013) with alignments of scoria cones and lava flows covering systems of tectonic fractures, suggesting that magmatic activity in the area is young, although these eruptive products have not been dated. High crustal V_P/V_S ratios (> 2.0) were also measured in the area using receiver functions by Hammond et al. (2011) and were interpreted as due to the presence of magmatic fluids between EA and TA.

At the center, the AP is dissected by a system of ~NS-striking faults (Figure 1b). Seismic catalogs from temporary networks in Afar (Belachew et al., 2011; Illsley-Kemp et al., 2018) showed seismicity along these fault systems indicating that the AP is tectonically active (Figure 1b). Seismicity at AP is characterized by low-magnitude earthquakes accompanying moderate earthquakes with $M_L > 5$. The only previously analyzed earthquake is the $M_L 5.0$ of 2 October 2007 (La Rosa et al. 2019). Fault modeling of InSAR data along with seismicity and structural data showed a combination of normal and left-lateral motions along ~NS-striking faults, which were interpreted as evidence that the overall right-lateral shear between the EA and TA segments is accommodated by oblique slip on ~NS-striking faults (Figure 1b) (La Rosa et al., 2019).

Figure 1 – Tectonics and seismicity of Northern Afar **a)** Magmatic segments in Afar, GPS full-spreading velocities w.r.t Nubia (Viltres et al., 2020) and seismic network used in this study (green reversed triangles). EA = Erta Ale, TA = Tat Ali, AP = Afrera Plain **b)** Seismicity of the Afrera Plain recorded during 2005-2013; green dots are the seismicity between 2005 and 2007 by Belachew et al. (2011); red dots are the seismicity during the 2007 seismic episode by La Rosa et al. (2019), and blue dots are the seismicity during 2011-2013 by

Accepted Article
Illsley-Kemp et al. (2018). The black lines are faults and fractures mapped in the area by La Rosa et al. (2019). The yellow diamonds are hydrothermal springs reported in the area by Brinckmann et al. (1970). c) Simplified kinematic model for the Afrera Plain by La Rosa et al. (2019).

3. InSAR and Seismic Data

We analyzed a vast dataset of SAR images by the European satellites ENVISAT and S1 covering the Afrera zone and spanning the time periods 2005-2010 and 2014-2019, respectively, to investigate how deformation is distributed across the linkage zone. We finally analyzed the local seismicity recorded by two temporary seismic networks active in Ethiopia during 2017-2018 (Figure 1a) (Doubre et al, 2017b; Keir et al., 2017; La Rosa et al., 2021).

3.1. InSAR Data processing

We formed 92 interferograms from SAR images of the ENVISAT satellite in both ascending (track 028) and descending (track 049) geometries from 2005 to 2010. ENVISAT interferograms were generated using the ROI_PAC software developed by JPL/Caltech (Rosen et al., 2004). Topographic phase contributions were removed using an external 3-arc sec (~90 m resolution) SRTM DEM (Farr et al., 2007). Interferograms were then filtered using a power spectrum filter (Goldstein & Werner, 1998) with strength of 0.6 and unwrapped using the ICU branch-cut algorithm (Goldstein et al., 1988). The unwrapped interferograms were then geocoded using the same SRTM DEM. We also produced 142 interferograms from S1 satellite images in both ascending and descending tracks (014 and 079) for the 2014-2019 period, using the JPL/Caltech/Stanford InSAR Scientific Computing Environment (ISCE) software package (Rosen et al., 2012). The SLCs co-registration and the topographic phase removal were performed using a 1-arc sec (~30 m resolution) SRTM DEM (Farr et al., 2007). Residual noise and decorrelation were then filtered with an adaptive power-spectral filter with strength of 0.5 (Goldstein & Werner, 1998). Interferograms were then unwrapped with the ICU branch-cut method (Goldstein et al., 1988) and geocoded to the 1-arc sec SRTM DEM. We processed interferometric pairs with both small perpendicular and temporal baselines, which in the case of ENVISAT implies using all the available satellite acquisitions, with the exception of few interferograms with large baselines or that are noisy (Figure S1). For S1, we processed almost all acquisitions between 2014 and 2016. Considering much more frequent acquisitions since 2016, we processed interferograms with small perpendicular baselines and spanning periods between 12 to 36 days, excluding some acquisitions with high level of noise (Figure S2).

3.2. InSAR Time-Series Analysis

In order to minimize sources of errors in the interferograms, we estimated time-series of cumulative satellite LOS displacements and their uncertainties for each InSAR track, using the Π -RATE software (Wang et al., 2012). We analyzed 51 interferograms for ENVISAT ascending track 028, 41 for ENVISAT descending track 049, 55 for S1 ascending track 014, and 87 for S1 descending track 079 (Figure S1 and S2). Before the time-series analysis, we multi-looked the S1 interferograms to a pixel size of 90m-by-90m to reduce noise, this is also the same resolution as for the ENVISAT interferograms. Unwrapping errors were identified in ENVISAT data by adopting a phase closure method on Minimum Spanning Trees (Wang et al., 2012), while the excellent level of coherence in S1 data and lack of dense fringe patterns ensure that there are no unwrapping mistakes in this study. Using a network approach, we applied orbital filtering to the geocoded interferograms by fitting them with a linear-function (Biggs et al., 2007). We also removed topographically-correlated atmospheric noise (Elliott et al., 2008) and applied an Atmospheric Phase Screen (APS) filter to minimize all other atmospheric disturbances (Ferretti et al., 2001). Abrupt displacements were also extracted from the time-series using the cross-correlation technique (Pagli et al., 2014) before applying the APS filter. To identify the time of abrupt displacements we analyzed the series of interferograms and local seismicity catalogues, and we found that other than the previously reported ML5 earthquake of 2 October 2007 (Figure S3a and b) (La Rosa et al., 2019), abrupt displacements occurred in January 2018 in the Afrera central fault system (Figure S3c and d). Figure S4 show the results of cross-correlation for the January 2018 episode. Another small sudden ground motion also occurred in February 2018 but only part of the signal is visible and some is covered by the Afrera Lake (Figure S3e and f). The signal is included in the time series but cross-correlation was not applied to it due to the lack multiple co-seismic independent interferograms covering just this event. This is described with further detail in section 3.2.2.

The only other sudden displacements in Afar during the observation period are the 2005-2010 intrusions at Dabbahu (Ebinger et al., 2008; Barnie et al., 2016a) and the 2017 Erta Ale eruption (Xu et al., 2017; Moore et al., 2019), both of which occurred outside of our study area. Dabbahu is ~100 km away from the AP and our ENVISAT dataset starts from October 2005, hence after the main intrusion occurred. The area affected by the Erta Ale volcano deformation is to the north of the AP but outside of the selected study area. After abrupt displacements were identified and extracted from the interferograms (Figure S4), we

then applied APS using a combination of temporal high-pass and spatial low-pass filter with a temporal Gaussian filter with length of 0.5 years followed by a spatial Butterworth filter with low-pass cutoff estimated from the variance-covariance matrix of the spatially correlated noise. We then estimated time-series of incremental displacements and their uncertainties on a pixel-by-pixel basis using a Laplacian smoothing with interferograms after APS removal (Wang et al., 2012). We selected a smoothing factor that minimizes the trade-off between the solution roughness and the Residual Sum of Squares (RSS) of the displacements (Figure S5). Our tests (Figure S5) show the results are reliable because the inverted time-series are consistent with the raw observations with varying smoothing factors. Finally, the aforementioned estimated abrupt displacements of October 2007 and January 2018 were added back to give the resultant time-series.

3.2.1. Time-Series Results: 2005-2010

The cumulative time-series show three deforming areas of range increase (positive values) in both ascending and descending ENVISAT tracks (Figure 2 and 3) with deformation patterns corresponding to en-echelon ~NS-striking faults mapped in the area. A series of profiles of cumulative InSAR displacement across different faults are displayed in Figure 4 and S6, showing that the InSAR deformation clearly match the faults. This demonstrates that a relationship between the InSAR deformation patterns and active faults exists. The range increase in both tracks is consistent with dominant normal faulting with down-dip motion of the hanging-walls along 2-5 km-long faults.

The time-series of cumulative displacements also show that deformation is accommodated in different manners across the AP (Figures 2-4 and S6). We see sudden steps in ground motion indicating stick-slip faulting during the October 2007 earthquake (pixel 1 in Figure 3; Profiles A and B in Figures 4 and S6). However, we also see time-progressive continuous displacements indicating creep occurring along different sub-parallel faults during the observation period (pixels 2 and 3 in Figure 3; Profile C in Figure 4 and Figure S6g-j). The total range increase along abruptly deforming faults is comparable to those deforming continuously at pixel 2 (~30-40 mm), showing that stick-slip faulting accommodates as much strain as fault creep during 2005-2009. Conversely, less deformation is taken up by the fault at pixel 3 (~10-30 mm) (pixel 3 in Figure 3; Profile D in Figure S6).

Figure 2 – Maps of LOS cumulative displacement at selected epochs (~1-year interval) from ENVISAT data. The blue, numbered asterisks show the location of the time-series shown in Figure 3. Patterns of range increase (white-to-red colors) across major faults are observed in both ascending in descending tracks, suggesting faulting with dominant normal kinematics.

The InSAR observations show that faulting along ~NS-striking faults is the dominant mode of deformation in the AP during 2005-2010. This is also consistent with InSAR and seismicity models of the ML 5 earthquake in 2007 (La Rosa et al., 2019). To further investigate the relationship between seismicity during 2005-2010 and the InSAR displacements, we analyzed the seismicity in the three deforming areas as identified by InSAR using local catalogues (Figure 3) (Belachew et al. 2011; La Rosa et al. 2019). Figure 3 shows that the highest number of earthquakes occurred in the central fault system during the October 2007 seismic sequence when the ML5 also happened. Few earthquakes are also observed in areas around pixels 2 and 3 indicating that fault creep is likely associated with minor seismicity.

Figure 3 – Time-series of cumulative LOS displacements (including sudden displacements) extracted from pixels as shown in Figure 2. a) and c) show the cumulative displacements at the last epoch. The blue triangles in b) and d) show the raw time-series while the black dots are the filtered ones. The error bars are scaled and the scale is reported in the legend. Histograms are the number of earthquakes during the InSAR observation period and the red line marks the ML5 earthquake of 2 October 2007.

Figure 4 - ENVISAT time-series of cumulative LOS displacements and active faults along different profiles. a) Locations of profiles in ascending track 028 and mapped faults (black lines). The time-series clearly shows that both sudden (panels b-c) and time-progressive deformation (panels d) occur corresponding to the faults. The major faults that were mapped are also shown in cross section (black lines). Further time-series are shown in Figure S6.

3.2.2. Time-Series Results: 2014-2019

The S1 cumulative time-series show two main deforming areas of range increase both in the ascending and descending tracks (Figure 5 and 6). The deformation patterns are consistent with motions along short, ~NS-striking fault planes. A deformation pattern observed during the 2005-2010 period also continued deforming in 2014-2019 (pixels 2 in Figure 2 and 3), and new abrupt displacements also occurred (pixel 4 in Figure 5 and 6).

The time-series at pixel 4 (Figure 5 and 6) shows that the abrupt displacement occurred to the east of the October 2007 episode, confirming that extension in the center of Afrera is accommodated by stick-slip along a number of fault segments. The January 2018 displacement at pixel 4 also corresponds to a seismic sequence including two $M_L \sim 5$ earthquakes from 10 January 2018 to the 31 January 2018 (the seismicity is analyzed in section 5). To the east of this event, the time-series at pixel 2 shows that fault creep is still ongoing similar to what was observed during 2005-2010 (Figure 5 and 6). The time-series in the descending track show higher displacements in the eastern sector and near pixel 2 (~40 mm) with respect to those measured in the same area in the ascending track (~20 mm)

(Figure 5 and 6). This is due to interaction with another abrupt displacement that occurred east of pixel 2 and north of the Afrera Lake in February 2018 (Figure S3e and f), when a ~19 mm of range increase along a short, ~NNW-striking fault is observed. This sector of the study area hosts west-dipping faults bounding the eastern shore of the lake (Bonatti et al. 2017). The pattern is small and is observed just in the descending track likely because the normal and lateral component of the fault motion add constructively in the descending track but not in the ascending one. Yet the presence of the signal in two independent interferograms confirms that the signal is real. We tried to extract the February 2018 abrupt displacement before the APS filter using the cross-correlation as done for the October 2007 and January 2018 episodes. However, this was not possible for a series of reasons, primarily due to the fact that we do not have two interferograms spanning the February 2018 event only (January 2018 event is included), the magnitude of the signal is small and its spatial pattern can't be fully observed and it is partly covered by the lake (Figure S3e and f). We decided to include the February 2018 in the time-series analysis for completeness but without applying the cross-correlation, hence the abrupt ground motion does not show as an offset in Figure 6d but it is smoothed by the APS filter. Therefore, displacements at the eastern tip of the AP are higher than those observed during 2005-2010 because of the February 2018 episode (Figure 5 and 6).

Figure 5 - Maps of cumulative displacements respect to the satellite LOS at different epochs from S1 data. A gap in 2017 is present in the ascending track due to lack of acquisitions in that period. The blue, numbered asterisks in the maps show the location of the time-series in Figure 6.

Finally, the time-series from ascending track 014 also show some other patterns of range increase corresponding to mapped faults in the western sector of the AP (Figure 5a-f), where time-progressive displacement signals were observed during 2005-2010 (pixel 3 in Figure 2-4 and S6). Such patterns are likely related to ongoing deformation along the same faults as observed in ENVISAT data. Indeed, similarly to ENVISAT, the displacements in S1 descending track, are lower than those measured in the ascending track, if not completely zero. This could be due to the oblique fault kinematics and the fact that the strike-slip and normal-slip components add constructively in descending LOS but cancel out in ascending LOS.

Figure 6 - Time-series of cumulative displacements (including sudden displacements) in the satellite LOS extracted from pixels in Figure 4. a), c) show the cumulative displacements at the last epoch. The blue triangles in b), d) show the raw time-series while the black dots show the filtered ones. The error bars are scaled and the scale is reported in the legend. The red line marks the time of the seismic event in January 2018.

4. InSAR Modeling

4.1 Modeling of the January 2018 earthquake

We modelled the displacement observed in January 2018 as fault slip by jointly inverting two S1 independent interferograms from both ascending (014) and descending (079) orbits assuming an Okada shear dislocation (Okada, 1985) with uniform slip across the fault plane in a conventional elastic half-space with a Poisson's ratio of 0.25 and a shear modulus (μ) of 3.2×10^{10} Pa. For the modeling, we used a Monte Carlo simulated annealing algorithm, followed by a derivative based procedure, (Cervelli et al., 2001; Jonsson et al., 2002; Pagli et al., 2012). We inverted both the observed interferograms and those extracted with cross-correlation. Initially, we inverted two 36-days long independent interferograms, (this is referred as Model 1). The interferograms were sub-sampled using the quadtree partitioning algorithm from Jonsson et al. (2002). For Model 1, we set narrow bounds on the location and strike of the fault (between N330°E and N30°E) using the strike of mapped structures in the area as a priori knowledge, while we let the other parameters free to vary. The best-fit Model 1 solution consists of a ~NS-striking fault (N357°E) dipping to the east with an angle of 67° (Figure S7). The fault is oblique with left-lateral (~33 mm) and normal (~45 mm) components (Figure S7). Model 1 has relatively low Root-Mean-Square (RMS)

Accepted Article

residuals of ~3 mm in both ascending and descending tracks (Table S1). However, the fault plane has an anomalous aspect ratio with a width of ~10 km and a length of 3.5 km (Figure S7 and table S1). Furthermore, the best-fit fault width corresponds to the upper bound of the search window. We then constrain the bounds on the fault width to be between 1-3 km (this is referred as Model 2) (Figure S8). Model 2 shows that a solution with a 3 km fault width exists and the model is again an oblique left-lateral fault with geometry and kinematics comparable to Model 1. The fault strikes ~N358°E and dips ~76° to the east. The slip has 69 mm of left-lateral and ~55 mm of normal components, resulting in a geodetic M_w 5 (Figure S8 table S2). Model 1 and Model 2 show similar RMS residuals of ~3 mm in both ascending and descending tracks (Table S2), yet Model 2 has a geologically reasonable fault aspect ratio (Figure S8).

Finally, we also inverted the January 2018 displacement signals as extracted from the time-series processing using the cross-correlation method (this is referred as Model 3). This allowed us to run the inversion minimizing the noise of the observed interferograms. The cross-correlated interferograms have been again quadtree partitioned (Jonsson et al., 2002). For the modeling, we again set relatively large bounds, except for the fault strike. Model 3 is again an oblique left-lateral fault striking N359°E and dipping to the east with an angle of ~68°. The fault length is 3.6 km-long and 4.8 km-wide (Figure 7 and Table S3). The fault slip has a dominant normal component of ~39 mm associated with a left-lateral slip of 13 mm. Model 3 has RMS residuals comparable to the previous solutions and equal to 2.7 mm and 3.2 mm in ascending and descending tracks, respectively (Table S3). The geodetic moment is 2.3×10^{16} Nm corresponding to a M_w 4.9 earthquake (Table S3). We also calculated the uncertainties associated with each model parameter by adopting the Monte Carlo simulation of correlated noise (Wright et al., 2003; Wang et al., 2014). We used the variance-covariance matrices of the input data to create 100 simulations of spatially correlated random noise. Such simulations have then been added to the input data and inverted (Figure S9). The 90% Confidence Interval (CI) for each parameter has been calculated from the distribution of the 100 solutions (Table S4). The 90% C.I. for the fault length and width range between 3.5-3.7 km and 4.2-5.4 km, respectively. Normal slip is very well constrained with a 90% C.I. of 3.8-4.1 cm, as also the strike-slip component with a 90% C.I. of 1.1-1.5.

To summarize, all the models show similar fault kinematics characterized by oblique left-lateral slip along ~NS-striking faults. The low variability in strike, kinematics and

Accepted Article

magnitude suggests that these parameters are rather well constrained. Using the cross-correlation (Model 3) has shown a great improvement in the quality of the input data, reducing the noise and the related local minima in the miss-fit space, and allowing the inversion for a better research of the global minimum. This is also shown by the very low variability in the fault parameters shown by the 100 Monte Carlo simulations (Figure S9) and by the narrow 90% CI for the best-fit solution (Table S4). Models 2 and 3 have similar fault geometries and kinematics, however, since no constraints have been imposed to the research across the model-misfit space in Model 3, we favor that solution. The kinematics of Model 3 is also similar to the event of October 2007, suggesting that oblique slip along ~NS-striking is the dominant mode of deformation in the central faults of the AP.

Figure 7 – Best-fit fault model (Model 3). a, b) cross-correlated deformation. c, d) model and e, f) residuals. The red beachball is the geodetic focal mechanism while the red square is the fault plane. The red dashed line is the projection of the fault top at surface. The two, orange stars are the major earthquakes occurred in January 2018.

4.2 Modeling of time-progressive displacement

We also modelled a creeping fault to understand the geometry and kinematics of these types of deformation. For the modeling we selected the creeping fault just north of the Afrera lake (pattern 2 in Figure 2 and 3) because it is far from other abrupt displacements. We jointly inverted the cumulative displacements between 2005 and 2010 of two InSAR ascending and descending tracks, using the same algorithms as for the stick-slip fault model. Our best-fit model (Figure S10 and Table S5) consists of an oblique left-lateral fault, striking ~NS and dipping ~64° to the east. The fault is 5.7 km-long, 4 km-wide and is located at a depth of 0.9 km, perfectly matching a mapped fault in the area (Figure 4). The fault accommodated ~86 mm and ~40 mm of left-lateral and dip-slip, respectively, during 2005-2010, which would correspond to a MW5.2 earthquake. The creeping fault geometry, kinematics and magnitude are similar to the stick-slip faults across the Afrera linkage-zone.

5. Seismic Analysis

To better characterize the stick-slip events, we analyzed the seismicity accompanying the fault slip identified by InSAR in January 2018 and recorded by the seismic network deployed in Afar in 2017-2018 (Dobre et al., 2017b; Keir et al., 2017; La Rosa et al., 2021). We inspected one month of continuous seismic recordings, from 1 January to 31 January 2018 to identify all the earthquakes during that period. We found a total of 499 earthquakes with the first P-wave arrival at station N009 (located at Afrera) and manually picked both P- and S-waves for earthquakes recorded by four or more stations. We then located the earthquakes using the Oct-Tree search algorithm implemented into the NLLoc software (Lomax et al., 2000) and a 2.5D velocity model of Afar. We finally estimated local magnitudes (ML) by measuring the zero-to-peak amplitude on simulated Wood Anderson seismometers, and applying the distance correction for the Danakil region from Illsley-Kemp et al. (2017).

All the 499 located earthquakes cluster at the AP, along the main NNW-trending fault system and occur within the upper crust (1-10 km) (Figure 8 and Table S6) with average horizontal and vertical errors of ± 2.8 km and ± 2.2 km, respectively (Table S6). The seismic sequence started the 10 January 2018 with a main-shocks of $ML \sim 5.2 \pm 0.3$ at depth of 9 ± 4 km (Table S6). The main-shock was followed by several aftershocks with $ML > 4.5$ along with another shallower (~ 2 km) $ML 5.1 \pm 0.4$ on the 11 January (Figure 8 and Table S6). The hypocentral locations are consistent with the InSAR time-series and modeling and indicate that two major earthquakes occurred. However, just a single fault was assumed in the InSAR

modeling as the two events could not be separated temporally in both ascending and descending tracks. Since the depth of the ML5.1 on 11 January was shallower (2.6 km) than the ML5.2 main-shock on 10 January (~ 9 km), it is likely that the displacement captured by InSAR is mainly due to the shallow earthquake, while the deeper ML5.2 does not contribute much to the surface displacement. To test this hypothesis, we produced two simulated interferograms assuming an Okada shear dislocation source having the top edge located at a depth of 9 km. For the simulation, we used the same homogeneous elastic half-space, fault geometry and kinematics of our preferred Model 3. We then set a fault slip of 134.5 mm, corresponding to a M_w 5.2 and approximately comparable to the ML5.2 calculated from seismic data. As can be seen in Figure S11, the simulations show negligible surface LOS displacements of 3.5 mm. This supports the hypothesis the only the ML5.1 of January 2018 contributes to the observed InSAR displacement, as also indicated by the very good correspondence between the hypocentral depth estimated from both InSAR inversion (2.6 km) and seismic data (2.0 km) for the 11 January earthquake.

The cumulative seismic moment release (Figure 8b) shows earthquakes occurring in the two days (8 and 9 January 2018) preceding the main earthquake. We attempted to process focal mechanisms for the earthquakes with $ML > 4.5$. However, due to the large azimuthal gaps of the seismic network in the study area, we have not been able to obtain unambiguous solutions. The majority of the aftershocks following the major earthquakes are shifted to the west (Figure 8a) likely suggesting that some small slip along nearby fault segments was triggered by the mainshock. We verified this by calculating the related Coulomb Stress Changes (CSC) (See section 6 and Figure S12).

Figure 8 – a) Seismicity located in Afrera between 1 and 31 January 2018 with fault and fractures (black lines). b) Cumulative seismic moment release and number of earthquakes during the same time-period. The two red lines in b) mark the two major events of 10 and 11 January. The histogram plot has a binning of 12 hours.

6. Coulomb Stress Changes (CSC) calculation

Earthquakes modify the stress conditions on nearby faults by either promoting or inhibiting slip (e.g. King et al., 1994; Harris, 1998; Lin & Stein, 2004; Toda et al., 2005). These stress changes can be quantified with the Coulomb failure criterion, whereby positive Coulomb stress changes caused by a fault slip (called the source fault) on a pre-stressed fault (called the receiver fault) can bring it to fail, while negative Coulomb stress changes unload faults inhibiting their rupture. We explore whether some stress-triggering effect occurred between the three major earthquakes, the $M_L 5$ in 2007 and the two $M_L \sim 5$ in 2018. For the Coulomb Stress Changes (CSC) calculation we used the Coulomb 3 software (<https://www.usgs.gov/software/coulomb-3>), and faults are modeled as Okada shear

dislocations within a uniform, elastic half-space with the same elastic moduli as used in the InSAR modeling. The geometry and kinematics of both source and receiver faults were set based on the InSAR modeling results (La Rosa et al., 2019 and this study).

We first analyzed the effect of the 2007 earthquake (source fault) on two receiver faults of January 2018. As the 2018 deeper event was not modeled by InSAR we assumed that the fault has the same geometry and kinematics as for the shallow 2018 earthquake. The CSC calculation (Figure S12a, b) shows that the 2007 earthquake caused negligible CSCs at depths greater than 6 km, therefore it is unlikely that it triggered the ML5.2 seismic event of January 2018 as this occurred at ~9 km depth. Furthermore, the 2007 earthquake caused a negative stress change (< -2 bar) at a depth of 2.6 km, where the ML5.1 of January 2018 occurred (Figure S12a, b). The negative CSC means fault slip would have been inhibited. From this, in addition to the 2007 and 2018 seismic events being separated by a fair delay of 11 years, we conclude that the 2018 events were not triggered by the 2007 earthquake. Another factor such as tectonic strain accumulation is the likely cause of the 2018 seismic sequence.

We also calculated the CSC imparted by the ML5.2 earthquake on 10 January 2018 at ~9 km depth (source fault) on the shortly following ML5.1 earthquake on the 11 January 2018 at 2.6 km depth (receiver fault). Figure S12 (c and d) shows that the ML5.2 earthquake generated a positive stress change (> 5 bar) at the base of the receiver fault with values of 0.5 bar at 2.6 km depth where the receiver fault hypocenter is positioned. Also, the area under positive CSC at the surface fits well with the aftershock distribution. These observations indicate that the CSCs caused by the deeper earthquake on 10 January 2018 triggered the shallower earthquake on 11 January 2018.

7. Discussion

We used InSAR time-series and modeling, along with seismic data and CSCs calculations to document the present kinematics of the AP linkage zone in Afar. This dataset, combined with the previous study on the AP (La Rosa et al., 2019), provides a detailed picture of how the deformation is distributed across the linkage zone formed by the interaction of the EA and TA magmatic segments. We show that en-echelon, ~NS-striking faults accommodate deformation at the AP. In the analyzed time-period, different individual faults are observed to be active at different time periods suggesting that deformation is not

limited to the central fault system (La Rosa et al., 2019) but instead it occurs on multiple faults with different behaviors across the linkage zone.

The major episodic displacements observed at the AP match the surface expression of mapped east-dipping faults. This is also supported by the east-dipping faults modeled from InSAR data for the major earthquakes that occurred in October 2007 (La Rosa et al., 2019) and January 2018. In addition, abrupt slip also occurs along west-dipping faults near the shore of the Afrera Lake in February 2018. This is also in agreement with field observations of dominant west-dipping faults along the eastern shore of the Afrera Lake (Bonatti et al., 2017). Overall, this indicates that extension at AP is mainly accommodated through dominant east-dipping faulting while active west-dipping faults characterize the eastern-most sector, where the AP connect to the TA segment.

The faults in Afrera also exhibit varying types of temporal behavior. Both the time-series and the individual interferograms show that abrupt fault slip events characterize the central fault system of the AP, suggesting that these fault segments have a dominant stick-slip behavior. Here, various fault segments accommodated deformation at different times with similar kinematics, fault size and timescales of seismic sequences that included the three largest earthquakes of $M_L > 5.0$. The most recent seismic sequence of January 2018 includes two $M_L > 5.0$ along with several $M_L > 4.5$ earthquakes. The best-fit InSAR model shows that fault slip occurs along a shallow oblique fault striking in a \sim NS direction and dipping to the east (Figure 7). The two largest earthquakes perfectly correspond to the area with the highest displacement observed with InSAR but just the second shallower (2.6 km) $M_L \sim 5$ of 11 January likely contributed to the observed surface displacement.

Stress triggering induced by the co-seismic fault slips was explored using the CSCs modeling but the calculations show that either negative or negligible stress changes were imparted by the 2007 fault onto the 2018 faults (Figure S12a, b). These results, along with the long time-span between the seismic episodes, lead us to exclude any stress triggering from the 2007 earthquake. Conversely, the doublet \sim MW5 earthquakes in January 2018 is a likely CSC triggering case (Figure S12c, d). Positive CSC were caused by the earlier and deeper earthquake onto the shallower fault. Also, the area of positive CSC explains well the peculiar aftershocks distribution, all to the west of the faults.

Faults close to the edges of the linkage zone display both time-progressive and abrupt displacements. The time-progressive displacements shown by the time-series at pixel 2, 3 (Figure 2-6) and profiles in figures S6g-h indicate that these faults creep continuously. We modelled the time-progressive deformation around pattern 2 showing that the creeping fault has again oblique left-lateral kinematics (Figure S10), similar to those deforming by stick-slip, and accommodates the same tectonics. Additionally, seismic records from Belachew et al. (2011) and Illsley-Kemp et al. (2018) along with relocated seismicity in La Rosa et al. (2019) show low magnitude earthquakes occurring in these areas during 2005-2009 and 2011-2013 (Figure 1 and 3). It is thus possible that the fault creep is not aseismic, but instead associated with micro-seismicity. Conversely, a west-dipping fault at the eastern tip of the AP showed abrupt displacements in February 2018 (Figure S3e, f and Figure 5) indicating that some faults could creep and others stick-slip.

It is well known that several types of fault behavior can co-exist along different portion of the same fault system or alternate in time along the same fault segment (Dobre & Peltzer, 2007; Harris, 2017). One of the best examples is the San Andreas fault where these phenomena have been well documented (e.g. de Michele et al., 2011; Sammis et al., 2016; Harris, 2017; Rousset et al., 2019). The fault behavior can be influenced by a wide range of factors encompassing temperature, presence of fluids, fault lithology or a combination of these (e.g. Byerlee & Brace, 1968, 1970; Byerlee, 1993; Vidale & Shearer, 2006; Dobre & Peltzer, 2007; Aochi et al., 2014; Harris, 2017). It has been shown that high temperatures in the deeper portions (> 15 km) of a fault zone may change its rheological properties favoring fault creep (e.g. Brace & Byerlee, 1970; Harris, 2017). Similarly, shallower hydrothermal circulation resulting from the interplay between fluids and positive thermal anomalies alters the fault rocks and generates phyllosilicates that weaken the fault zone in the upper crust and reduce its shear strength, favoring fault creep (e.g. Wintsch et al., 1995; Moore & Rymer, 2007). Conversely, an increase in the pressure of fluids circulating within the fault zone may induce significant fault slip on pre-stressed faults and therefore cause seismicity (Byerlee, 1993; Becken et al., 2011; Vidale & Shearer, 2006; Aochi et al., 2014; Harris, 2017; Ross et al., 2020). Overall, the AP transfer zone links two en-echelon magmatic segments by oblique slip on multiple en-echelon faults. We primarily observed stick-slip fault behavior in the center of the linkage zone (Brinckmann et al., 1970; Bonatti et al., 2017). Conversely, we observe a combination of creep and stick-slip at the edges of the linkage zone, in the vicinity of the magmatic segments and where hot springs exist, close to the eastern faults. The

observed variability of fault behavior, the results of the CSCs modeling, and the presence of hot-springs suggest that the kinematics of the Afrera rift-linkage zone is the result of the interaction between extensional tectonics, elevated heat flow and presence of fluids near the magmatic segments which influences the fault behavior, either facilitating fault creep, or promoting fault rupture by generating over-pressures on the faults. This hypothesis is also supported by independent geophysical evidences which indicate the presence of magmatic fluids below Afrera (Hammond et al., 2011).

8. Conclusion

In this study, we provided one of the few direct observations on how deformation is distributed across a linkage zone between two active magmatic segments. We combined a vast InSAR dataset from ENVISAT and Sentinel-1 satellites, spanning 2005-2010 and 2014-2019, respectively, with local seismic recordings from the Afar rift. We show that deformation at the AP, between the EA and TA segments, is accommodated by several en-echelon, ~NS-striking, oblique faults, which are arranged in two main structural architectures: dominant east-dipping faults characterize the center of the AP while dominant west-dipping faults are observed close to the eastern edge, where the AP meets the TA segment. Various fault segments are active at different time-periods, showing great variability in their behavior. The faults segments at the center of the AP show a dominant stick-slip behavior characterized by episodic slip events associated with $M_L \geq 5$ earthquakes and related seismic sequences. Conversely, heterogeneous fault behavior encompassing creep, micro-seismicity and minor episodic events characterizes the eastern tip. Here, a strong hydrothermal activity with hot springs and pools have been observed by Brinckmann et al. (1970) and Bonatti et al. (2017).

Our observations expand on our previous study showing the time-evolving behavior of fault segments at the AP (La Rosa et al., 2019). These new results support the kinematic model of rift-linkage that we proposed for the AP where a right-lateral, NW-SE-trending transfer zone is accommodating deformation between the EA and TA segments. Within the middle of the transfer zone, ~NS-trending oblique stick-slip faults accommodate most of deformation. In contrast, near the edges of the transfer zone there is also deformation by fault creep, where we interpret that heat flow and hydrothermal activity influence the fault behavior and allow fault creep.

Acknowledgements

This study was developed in the framework of the PhD project of A.L.R. (XXXIII cycle of the Dottorato Regionale Pegaso in Earth Sciences) and is supported by the Ministero Università e Ricerca (MiUR) through PRIN grant 2017P9AT72. A.L.R. and C.P. acknowledge partial support by the University of Pisa grant PRA_2018_19. H.W. was supported by the NFSC project (41672225). ENVISAT ASAR and Sentinel-1 IW SLCs are provided by the ESA Online Dissemination (ENVISAT) (<https://esar-ds.eo.esa.int/oads/access>) and by the Copernicus Open Access Hub (Sentinel-1) (<https://scihub.copernicus.eu/>). Seismic instruments were loaned by SEIS-UK. The facilities of SEIS-UK are supported by the Natural Environment Research Council (NERC) under agreement R8/H10/64. The temporary network deployment was part of an Actions-Marges and IStEP project (#2016-82). The continuous seismic data used in this study is archived on the IRIS-DMC (http://www.fdsn.org/networks/detail/YQ_2017/; http://www.fdsn.org/networks/detail/YP_2017/). The data will become fully open access once the 3-year embargo period finishes at the end of 2021. We thank the regional authorities of the Afar, Tigray and Amhara states for their administrative support. We also thank the wider staff body at the IGSSA of Addis Ababa University.

References

- Allken, V., Huismans, R. S., & Thieulot, C. (2012). Factors controlling the mode of rift interaction in brittle-ductile coupled systems: A 3D numerical study. *Geochemistry, Geophysics, Geosystems*, 13(5), 1–18. <https://doi.org/10.1029/2012GC004077>
- Amelung, F., Oppenheimer, C., Segall, P., & Zebker, H. (2000). Ground deformation near Gada 'Ale Volcano, Afar, observed by Radar Interferometry. *Geophysical Research Letters*, 27(19), 3093–3096. <https://doi.org/10.1029/2000GL008497>
- Aochi, H., Poisson, B., Toussaint, R., Rachez, X., & Schmittbuhl, J. (2014). Self-induced seismicity due to fluid circulation along faults. *Geophysical Journal International*, 196(3), 1544–1563. <https://doi.org/10.1093/gji/ggt356>
- Barberi, F., & Varet, J. (1970). The Erta Ale volcanic range (Danakil depression, northern afar, ethiopia). *Bulletin Volcanologique*, 34(4), 848–917. <https://doi.org/10.1007/BF02596805>
- Barnie, T. D., Keir, D., Hamling, I., Hofmann, B., Belachew, M., Carn, S., Eastwell, D., Hammond, J. O. S., Ayele, A., Oppenheimer, C., Wright, T., (2016a). A multidisciplinary study of the final episode of the Manda Hararo dyke sequence, Ethiopia, and implications for trends in volcanism during the rifting cycle. *Geological Society London Special Publications*, 420, 149–163. <https://doi.org/10.1144/SP420.6>
- Barnie, T. D., Oppenheimer, C., & Pagli, C. (2016b). Does the lava lake of Erta 'Ale volcano respond to regional magmatic and tectonic events? An investigation using Earth

Observation data. Geological Society, London, Special Publications, 420(1), 181 LP – 208. <https://doi.org/10.1144/SP420.15>

- Becken, M., Ritter, O., Bedrosian, P. A., & Weckmann, U. (2011). Correlation between deep fluids, tremor and creep along the central San Andreas fault. *Nature*, 480(7375), 87–90. <https://doi.org/10.1038/nature10609>
- Belachew, M., Ebinger, C., Coté, D., Keir, D., Rowland, J. V., Hammond, J. O. S., & Ayele, A. (2011). Comparison of dike intrusions in an incipient seafloor-spreading segment in Afar, Ethiopia: Seismicity perspectives. *Journal of Geophysical Research: Solid Earth*, 116(6), 1–23. <https://doi.org/10.1029/2010JB007908>
- Beyene, A., & Abdelsalam, M. G. (2005). Tectonics of the Afar Depression: A review and synthesis. *Journal of African Earth Sciences*, 41(1–2), 41–59. <https://doi.org/10.1016/j.jafrearsci.2005.03.003>
- Biggs, J., Wright, T., Lu, Z., & Parsons, B. (2007). Multi-interferogram method for measuring interseismic deformation: Denali Fault, Alaska. *Geophysical Journal International*, 170(3), 1165–1179. <https://doi.org/10.1111/j.1365-246X.2007.03415.x>
- Bonatti, E., Gasperini, E., Vigliotti, L., Lupi, L., Vaselli, O., Polonia, A., & Gasperini, L. (2017). Lake Afrera, a structural depression in the Northern Afar Rift (Red Sea). *Heliyon*, 3(5), e00301. <https://doi.org/10.1016/j.heliyon.2017.e00301>
- Brace, W. F., & Byerlee, J. D. (1970). California earthquakes: Why only shallow focus? *Science*, 168(3939), 1573–1575. <https://doi.org/10.1126/science.168.3939.1573>
- Brandsdóttir, B., & Einarsson, P. (1979). Seismic activity associated with the September 1977 deflation of the Krafla central volcano in northeastern Iceland. *Journal of Volcanology and Geothermal Research*, 6(3–4), 197–212. [https://doi.org/10.1016/0377-0273\(79\)90001-5](https://doi.org/10.1016/0377-0273(79)90001-5)
- Brinckmann, J., Kading C., Knetsch, G., Kurten, M. Mayrhofer, H., Richter-Bernburg G. (1970) Geological Sketchmap of the Danakil Depression.
- Brune, S., Corti, G., & Ranalli, G. (2017). Controls of inherited lithospheric heterogeneity on rift linkage: Numerical and analog models of interaction between the Kenyan and Ethiopian rifts across the Turkana depression. *Tectonics*, 36(9), 1767–1786. <https://doi.org/10.1002/2017TC004739>
- Byerlee, J. (1993). Model for episodic flow of high-pressure water in fault zones before earthquakes. *Geology*, 21(4), 303–306. [https://doi.org/10.1130/0091-7613\(1993\)021<0303:MFEFOH>2.3.CO;2](https://doi.org/10.1130/0091-7613(1993)021<0303:MFEFOH>2.3.CO;2)
- Byerlee, J. D., & Brace, W. F. (1968). Stick Slip, Stable Sliding, and Earthquakes. Effect of Rock Type, Pressure, Strain Rate, and Stiffness. *Journal of Geophysical Research*, 73(18), 6031–6037.
- Corti, G. (2012). Evolution and characteristics of continental rifting: Analog modeling-inspired view and comparison with examples from the East African Rift System. *Tectonophysics*, 522–523(1), 1–33. <https://doi.org/10.1016/j.tecto.2011.06.010>

- de Michele, M., Raucoules, D., Rolandone, F., Briole, P., Salichon, J., Lemoine, A., & Aochi, H. (2011). Spatiotemporal evolution of surface creep in the Parkfield region of the San Andreas Fault (1993-2004) from synthetic aperture radar. *Earth and Planetary Science Letters*, 308(1–2), 141–150. <https://doi.org/10.1016/j.epsl.2011.05.049>
- Decriem, J., & Árnadóttir, T. (2012). Transient crustal deformation in the South Iceland seismic zone observed by GPS and InSAR during 2000-2008. *Tectonophysics*, 581(June 2000), 6–18. <https://doi.org/10.1016/j.tecto.2011.09.028>
- Dobre, C., Déprez, A., Masson, F., Socquet, A., Lewi, E., Grandin, R., Necessian, A., Ulrich, P., De Chaballier, J., Saad, I., Abayazid A., Peltzer, G., Delorme, A., Calais, E., & Wright T. (2017a). Current deformation in Central Afar and triple junction kinematics deduced from GPS and InSAR measurements. *Geophysical Journal International*, 208(2), 936–953. <https://doi.org/10.1093/gji/ggw434>
- Dobre, C., Leroy, S., & Keir, D. (2017b). Margin Afar [Data set]. International Federation of Digital Seismograph Networks. https://doi.org/10.7914/SN/YP_2017
- Dobre, C., & Peltzer, G. (2007). Fluid-controlled faulting process in the Asal Rift, Djibouti, from 8 yr of radar interferometry observations. *Geology*, 35, 69–72. <https://doi.org/10.1130/G23022A.1>
- Eagles, G., Gloaguen, R., & Ebinger, C. (2002). Kinematics of the Danakil microplate. *Earth and Planetary Science Letters*, 203(2), 607–620. [https://doi.org/10.1016/S0012-821X\(02\)00916-0](https://doi.org/10.1016/S0012-821X(02)00916-0)
- Ebinger, C. J., Keir, D., Ayele, A., Calais, E., Wright, T. J., Belachew, M., Hammond, J.O.S., Campbell, E., & Buck, W.R. (2008). Capturing magma intrusion and faulting processes during continental rupture: Seismicity of the Dabbahu (Afar) rift. *Geophysical Journal International*, 174(3), 1138–1152. <https://doi.org/10.1111/j.1365-246X.2008.03877.x>
- Einarsson, P. (2008). Plate boundaries, rift and transforms in Iceland. *Jokull*, 58(August).
- Einarsson, P., & Brandsdóttir, B. (1979). Seismological Evidences for Lateral Magma intrusion during the July 1978 Deflation of the Krafle Volcano in NE-Iceland.
- Elliott, J. R., Biggs, J., Parsons, B., & Wright, T. J. (2008). InSAR slip rate determination on the Altyn Tagh Fault, northern Tibet, in the presence of topographically correlated atmospheric delays. *Geophysical Research Letters*, 35(12), 1–5. <https://doi.org/10.1029/2008GL033659>
- Farr, T. G., Rosen, P., Caro, E., Crippen, R., Duren, R., Hensley, S., Kobrick, M., Paller, M., Rodriguez, E., Roth, L., Seal, D., Shaffer, S., Shimada, J., Umland, J., Werner, M., Oskin, M., Burbank D., Alsdorf, D. (2007). The Shuttle Radar Topography Mission. *Reviews of Geophysics*, 45. <https://doi.org/10.1029/2005RG000183>
- Ferretti, A., Prati, C., & Rocca, F. (2001). Permanent scatterers in SAR interferometry. *IEEE Transactions on Geoscience and Remote Sensing*, 39(1), 8–20. <https://doi.org/10.1109/36.898661>

- Field, L., Barnie, T., Blundy, J., Brooker, R. A., Keir, D., Lewi, E., & Saunders, K. (2012). Integrated field, satellite and petrological observations of the November 2010 eruption of Erta Ale. *Bulletin of Volcanology*, 74(10), 2251–2271. <https://doi.org/10.1007/s00445-012-0660-7>
- Geirsson, H., Lafemina, P., Rnadóttir, T., Sturkell, E., Sigmundsson, F., Travis, M., Shmidt, P., Lund, B., Hreinsdottir, S., Bennet, R. (2012). Volcano deformation at active plate boundaries: Deep magma accumulation at Hekla volcano and plate boundary deformation in south Iceland. *Journal of Geophysical Research B: Solid Earth*, 117(11), 1–18. <https://doi.org/10.1029/2012JB009400>
- Gerya, T. V. (2013). Three-dimensional thermomechanical modeling of oceanic spreading initiation and evolution. *Physics of the Earth and Planetary Interiors*, 214, 35–52. <https://doi.org/10.1016/j.pepi.2012.10.007>
- Goldstein, R. M., & Werner, C. L. (1998). Radar interferogram filtering for geophysical applications. *Geophysical Research Letters*, 25(21), 4035–4038. <https://doi.org/10.1029/1998GL900033>
- Goldstein, R. M., Zebker, H. A., & Werner, C. L. (1988). Satellite radar interferometry: Two-dimensional phase unwrapping. *Radio Science*, 23(4), 713–720. <https://doi.org/10.1029/RS023i004p00713>
- Harris, R. A. (1998). Introduction to special section: Stress triggers, stress shadows, and implications for seismic hazard. *Journal of Geophysical Research*, 103, 24,347–24,358. <https://doi.org/10.1029/98JB01576>
- Harris, R. A. (2017). Large earthquakes and creeping faults. *Reviews of Geophysics*, 55(1), 169–198. <https://doi.org/10.1002/2016RG000539>
- Hayward, N. J., & Ebinger, C. J. (1996). Variations in the along-axis segmentation of the Afar. *Tectonics*, 15(2), 1–14. <https://doi.org/10.1029/95TC02292>
- Illsley-Kemp, F., Bull, J. M., Keir, D., Gerya, T., Pagli, C., Gernon, T., Ayele, A., Goitom, B., Hammond, J.O.S., Kendall, J.M. (2018). Initiation of a Proto-transform Fault Prior to Seafloor Spreading. *Geochemistry, Geophysics, Geosystems*, 19(12), 4744–4756. <https://doi.org/10.1029/2018GC007947>
- Illsley-Kemp, F., Keir, D., Bull, J. M., Ayele, A., Hammond, J. O. S., Kendall, J. M., Gallacher, R.J., Gernon, T., Goitom, B. (2017). Local earthquake magnitude scale and b-value for the Danakil region of northern afar. *Bulletin of the Seismological Society of America*, 107(2), 521–531. <https://doi.org/10.1785/0120150253>
- Jonsson, S., Zebker, H., Segall, P., & Amelung, F. (2002). Mw7.1 Hector Mine, California, Earthquake, Estimated from Satellite Radar and GPS Measurements. *Bulletin of the Seismological Society of America*, 92(4), 1377–1389. <https://doi.org/10.1785/0120000922>
- Keir, D., Hamling, I. J., Ayele, A., Calais, E., Ebinger, C., Wright, T. J., Jacques E., Mohamed K., Hammond, J.O.S., Belachew, M., Baker, E., Rowland, J.V. Lewi, E., Bennati, L. (2009). Evidence for focused magmatic accretion at segment centers from lateral dike

injections captured beneath the Red Sea rift in Afar. *Geology*, 37(1), 59–62.
<https://doi.org/10.1130/G25147A.1>

Keir, D., Bastow, I. D., Pagli, C., & Chambers, E. L. (2013). The development of extension and magmatism in the Red Sea rift of Afar. *Tectonophysics*, 607, 98–114.
<https://doi.org/10.1016/j.tecto.2012.10.015>

Keir, D., Doubre, C., Leroy, S. (2017). Afar Margin Northern Profile. International Federation of Digital Seismograph Networks. https://doi.org/10.7914/SN/YQ_2017

King, G. C. P., Stein, R.S., and Lin, J. (1994). Static Stress Changes and the Triggering of Earthquakes. *Bulletin of the Seismological Society of America*, 84 (3), 935–953

La Rosa, A., Pagli, C., Keir, D., Sani, F., Corti, G., Wang, H., & Possee, D. (2019). Observing Oblique Slip During Rift Linkage in Northern Afar. *Geophysical Research Letters*, 46(19), 10782–10790. <https://doi.org/10.1029/2019GL084801>

La Rosa, A., Keir, D., Doubre, C., Sani, F., Corti, G., Leroy S., Ayele, A., & Pagli, C. (2021). Lower crustal earthquakes in the March 2018 sequence along the Western Margin of Afar. *Geochemistry, Geophysics, Geosystems*.
<https://doi.org/10.1029/2020GC009614>

Le Pourhiet, L., May, D. A., Huille, L., Watremez, L., & Leroy, S. (2017). A genetic link between transform and hyper-extended margins. *Earth and Planetary Science Letters*, 465, 184–192. <https://doi.org/10.1016/j.epsl.2017.02.043>

Leroy, S., Razin, P., Autin, J., Bache, F., d'Acremont, E., Watremez, L., et al. (2012). From rifting to oceanic spreading in the Gulf of Aden: A synthesis. *Arabian Journal of Geosciences*, 5(5), 859–901. <https://doi.org/10.1007/s12517-011-0475-4>

Lin, J. & Stein, R. S. (2004). Stress triggering in thrust and subduction earthquakes, and stress interaction between the southern San Andreas and nearby thrust and strike-slip faults. *Journal of Geophysical Research*, 109, B02303.
<https://doi.org/10.1029/2003JB002607>

Lomax, A., Virieux, J., Volant, P., & Berge-Thierry, C. (2000). Probabilistic Earthquake Location in 3D and Layered Models. In C. H. Thurber & N. Rabinowitz (Eds.), *Advances in Seismic Event Location* (pp. 101–134). Berlin: Springer.
https://doi.org/10.1007/978-94-015-9536-0_5

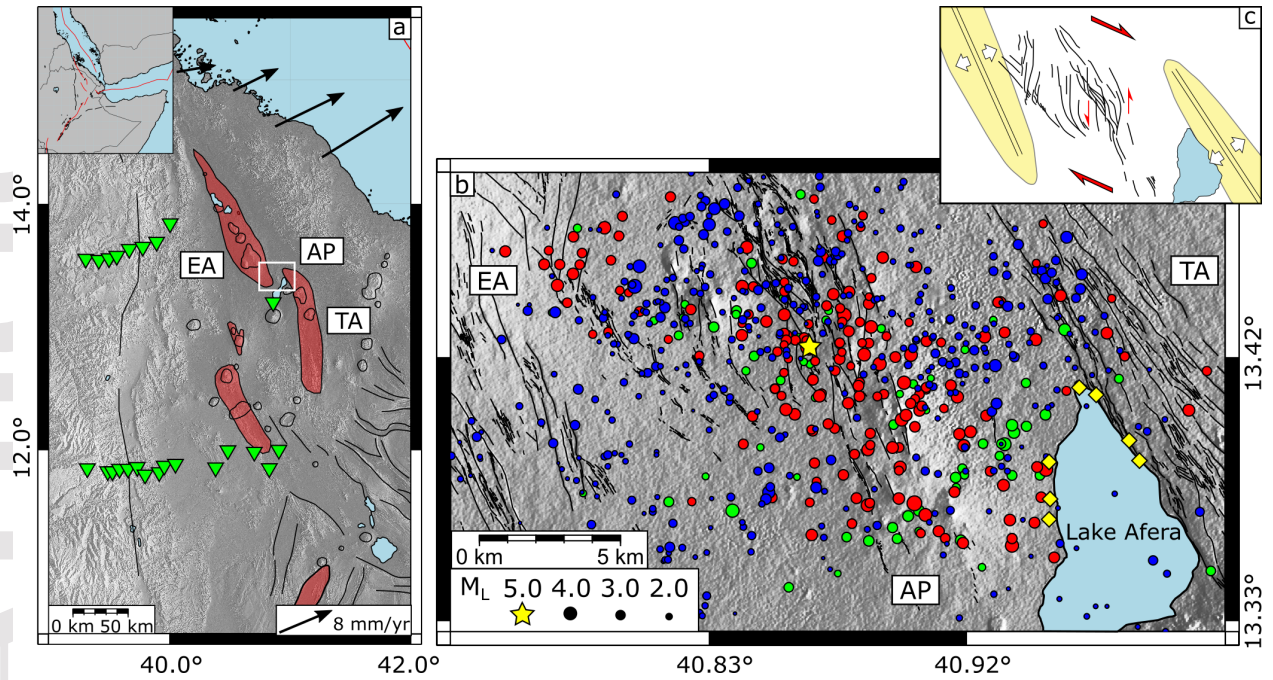
Manighetti, I., King, G. C. P., Gaudemer, Y., Scholz, C. H., and Doubre, C. (2001). Slip accumulation and lateral propagation of active normal faults in Afar. *Journal of Geophysical Research*, 106 (B7), 13667–13696.
<https://doi.org/10.1029/2000JB900471>.

Manighetti, I., Tapponnier, P., Gillot, P. Y., Jacques, E., Courtillot, V., Armijo, R., Ruegg, J. C., and King, G. (1998), Propagation of rifting along the Arabia–Somalia Plate Boundary: Into Afar, *Journal of Geophysical Research*, 103 (B3), 4947–4974,
<https://doi.org/10.1029/97JB02758>.

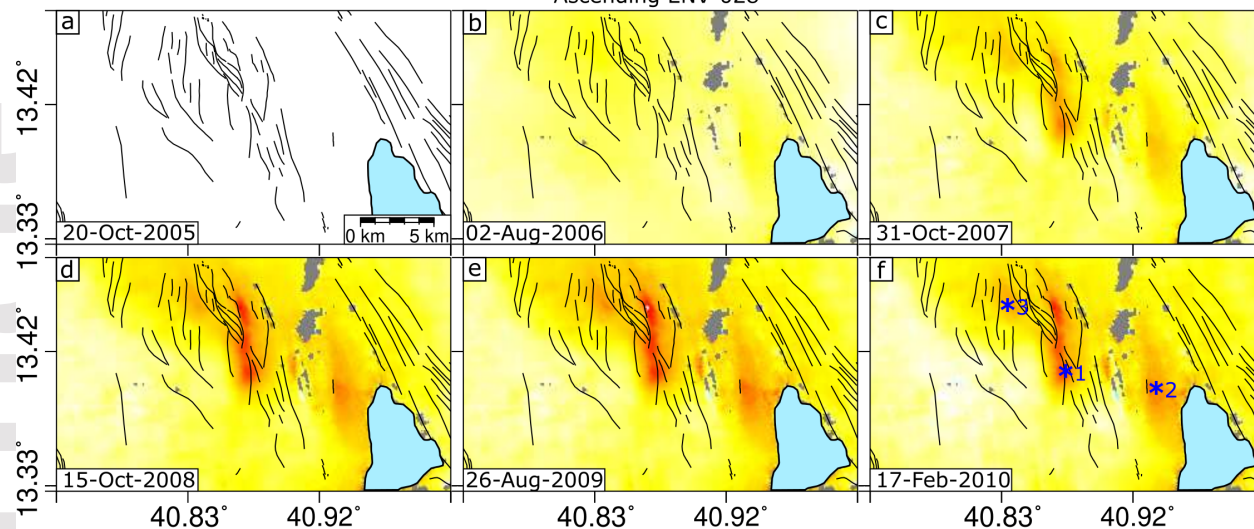
- Metzger, S., & Jónsson, S. (2014). Plate boundary deformation in North Iceland during 1992–2009 revealed by InSAR time-series analysis and GPS. *Tectonophysics*, 634, 127–138. <https://doi.org/10.1016/j.tecto.2014.07.027>
- Metzger, S., Jónsson, S., Danielsen, G., Hreinsdóttir, S., Jouanne, F., Giardini, D., & Villemín, T. (2013). Present kinematics of the tjörnes fracture zone, North Iceland, from campaign and continuous GPS measurements. *Geophysical Journal International*, 192(2), 441–455. <https://doi.org/10.1093/gji/ggs032>
- Moore, C., Wright, T., Hooper, A., & Biggs, J. (2019). The 2017 Eruption of Erta 'Ale Volcano, Ethiopia: Insights into the Shallow Axial Plumbing System of an Incipient Mid-Ocean Ridge. *Geochemistry, Geophysics, Geosystems*, 20(12), 5727–5743. <https://doi.org/10.1029/2019GC008692>
- Moore, D. E., & Rymer, M. J. (2007). Talc-bearing serpentinite and the creeping section of the San Andreas fault. *Nature*, 448(7155), 795–797. <https://doi.org/10.1038/nature06064>
- Nobile, A., Pagli, C., Keir, D., Wright, T. J., Ayele, A., Ruch, J., & Acocella, V. (2012). Dike-fault interaction during the 2004 Dallol intrusion at the northern edge of the Erta Ale Ridge (Afar, Ethiopia). *Geophysical Research Letters*, 39(19), 2–7. <https://doi.org/10.1029/2012GL053152>
- Okada, Y. (1985). Surface deformation due to shear and tensile faults in a half-space. *Bulletin of the Seismological Society of America*, 75(4), 1135–1153.
- Opheim, J. A., & Gudmundsson, A. (1989). Formation and geometry of fractures, and related volcanism, of the Krafla fissure swarm, northeast Iceland. *Geological Society of America Bulletin*, 101(12), 1608–1622. [https://doi.org/10.1130/0016-7606\(1989\)101<1608:FAGOFA>2.3.CO;2](https://doi.org/10.1130/0016-7606(1989)101<1608:FAGOFA>2.3.CO;2)
- Pagli, C., Wright, T. J., Ebinger, C. J., Yun, S.-H., Cann, J. R., Ayele, A., & Barnie, T. (2012). Shallow axial magma chamber at the slow-spreading Erta Ale Ridge. *Nature Geoscience*, 5(4), 284–288. <https://doi.org/10.1038/NGEO1414>
- Pagli, C., Wang, H., Wright, T. J., Calais, E., & Lewi, E. (2014). Current plate boundary deformation of the Afar rift from a 3-D velocity field inversion of InSAR and GPS. *Journal of Geophysical Research: Solid Earth*, 119, 8562–8575. <https://doi.org/10.1002/2014JB011391>
- Pagli, C., Yun, S.-H., Ebinger, C., Keir, D., & Wang, H. (2019). Strike-slip tectonics during rift linkage. *Geology*, 47(1), 31–34. <https://doi.org/10.1130/g45345.1>
- Rosen, P. A., Hensley, S., Peltzer, G., Simons, M. (2004). Updated Repeat Orbit Interferometry Package released. *Eos, Transactions, American Geophysical Union*, 85(5). <https://doi.org/10.1029/2004EO050004>
- Rosen, P. A., Gurrola, E. M., Sacco, G. F., & Zebker, H. (2012). The InSAR scientific computing environment. In *EUSAR 2012; 9th European Conference on Synthetic Aperture Radar* (pp. 730–733).

- Ross, Z. E., Cochran, E. S., Trugman, D. T., & Smith, J. D. (2020). 3D fault architecture controls the dynamism of earthquake swarms. *Science*, 368(June), 1357–1361. <https://doi.org/10.1126/science.abb0779>
- Rousset, B., Bürgmann, R., & Campillo, M. (2019). Slow slip events in the roots of the San Andreas fault. *Science Advances*, 5(2), 1–8. <https://doi.org/10.1126/sciadv.aav3274>
- Sammis, C. G., Smith, S. W., Nadeau, R. M., & Lippoldt, R. (2016). Relating transient seismicity to episodes of deep creep at Parkfield, California. *Bulletin of the Seismological Society of America*, 106(4), 1887–1899. <https://doi.org/10.1785/0120150224>
- Taylor, B., Goodliffe, A., & Martinez, F. (2009). Initiation of transform faults at rifted continental margins. *Comptes Rendus - Geoscience*, 341(5), 428–438. <https://doi.org/10.1016/j.crte.2008.08.010>
- Toda, S., Stein, R. S., Richards-Dinger K., and Bozkurt, S. (2005). Forecasting the evolution of seismicity in southern California: Animations built on earthquake stress transfer. *Journal of Geophysical Research*, 110, B05S16, <https://doi.org/10.1029/2004JB003415>
- Tapponier, P., & Varet, J. (1974) La zone de Mak'arrasou en Afar: un équivalent émergé des “failles transformantes” océanique. *C.R. Acad. Sci. Paris*, 278, 209–212.
- Vidale, J. E., & Shearer, P. M. (2006). A survey of 71 earthquake bursts across southern California: Exploring the role of pore fluid pressure fluctuations and aseismic slip as drivers. *Journal of Geophysical Research: Solid Earth*, 111(5), 1–12. <https://doi.org/10.1029/2005JB004034>
- Viltres, R., Jónsson, S., Ruch, J., Doubre, C., Reilinger, R., Floyd, M., & Ogubazghi, G. (2020). Kinematics and deformation of the southern Red Sea region from GPS observations. *Geophysical Journal International*, 221(3), 2143–2154. <https://doi.org/10.1093/gji/ggaa109>
- Wang, H., Wright, T. J., Yu, Y., Lin, H., Jiang, L., Li, C., & Qiu, G. (2012). InSAR reveals coastal subsidence in the Pearl River Delta, China. *Geophysical Journal International*, 191(3), 1119–1128. <https://doi.org/10.1111/j.1365-246X.2012.05687.x>
- Wang, H., Elliott, J. R., Craig, T. J., Wright, T. J., Liu-Zeng, J., & Hooper, A. (2014). Normal faulting sequence in the Pumqu-Xainza Rift constrained by InSAR and teleseismic body-wave seismology. *Geochemistry Geophysics Geosystems*, 15, 2947–2963. <https://doi.org/10.1002/2014GC005369>
- Wintsch, R. P., Christoffersen, R., & Kronenberg, A. K. (1995). Fluid-rock reaction weakening of fault zones. *Journal of Geophysical Research*, 100(B7). <https://doi.org/10.1029/94jb02622>
- Wright, T. J., Lu, Z., & Wicks, C. (2003). Source model for the Mw 6.7, 23 October 2002, Nenana Mountain Earthquake (Alaska) from InSAR. *Geophysical Research Letters*, 30(18), 30–33. <https://doi.org/10.1029/2003GL018014>

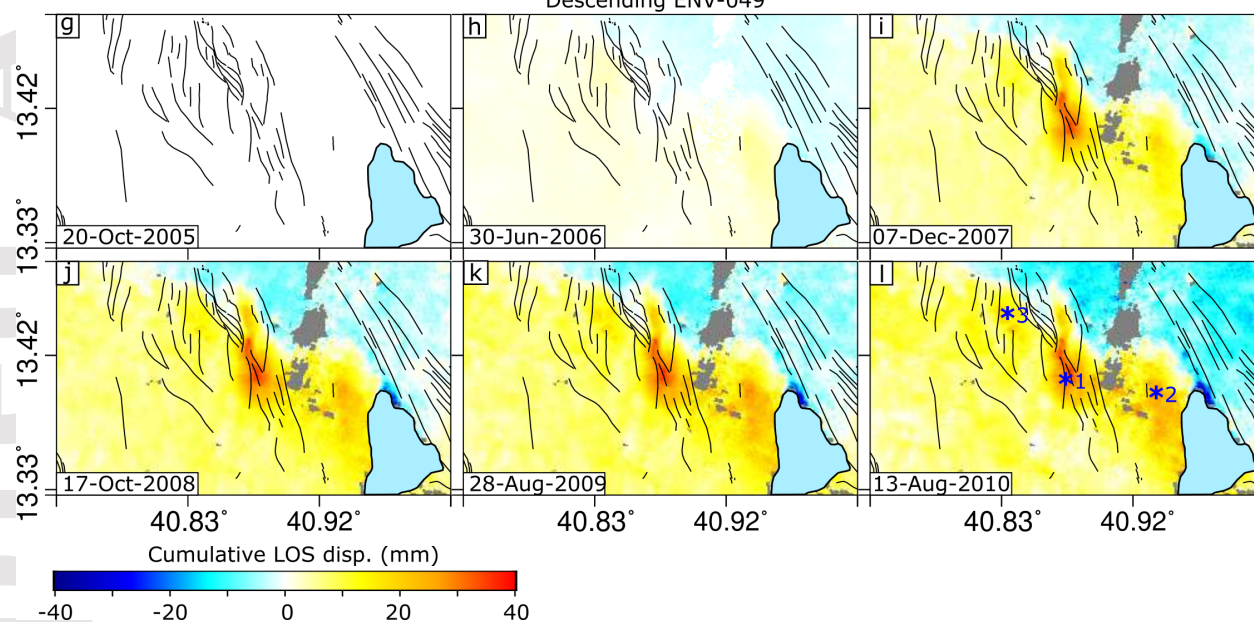
Xu, W., Rivalta, E., & Li, X. (2017). Magmatic architecture within a rift segment: Articulate axial magma storage at Erta Ale volcano, Ethiopia. *Earth and Planetary Science Letters*, 476, 79–86. <https://doi.org/10.1016/j.epsl.2017.07.051>

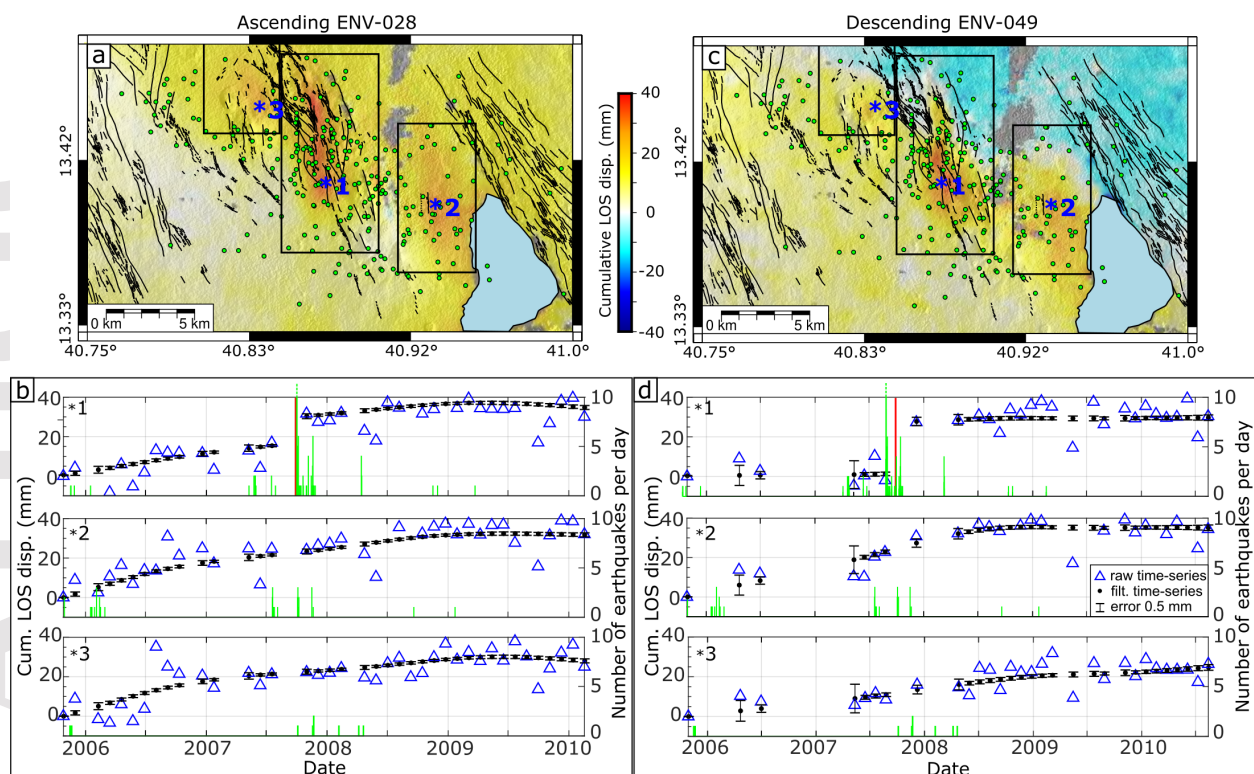


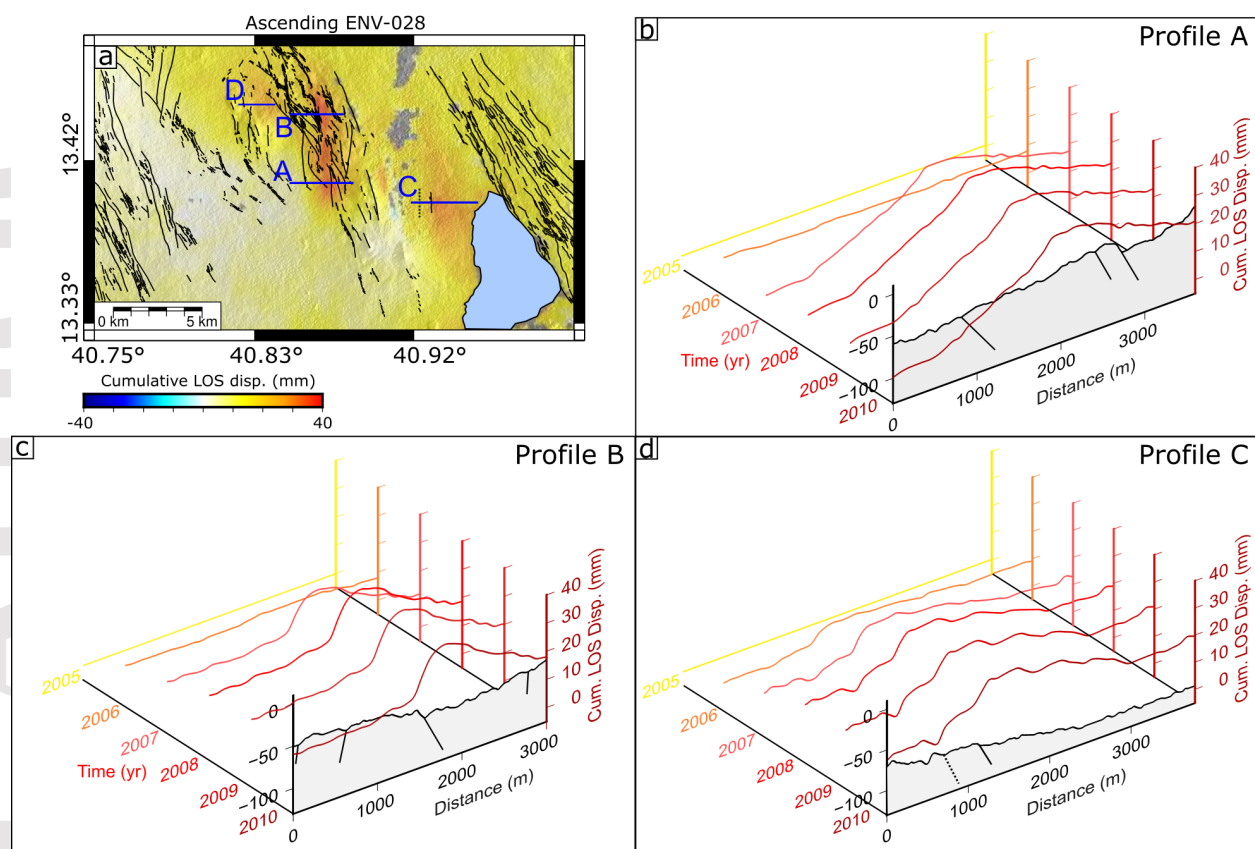
Ascending ENV-028



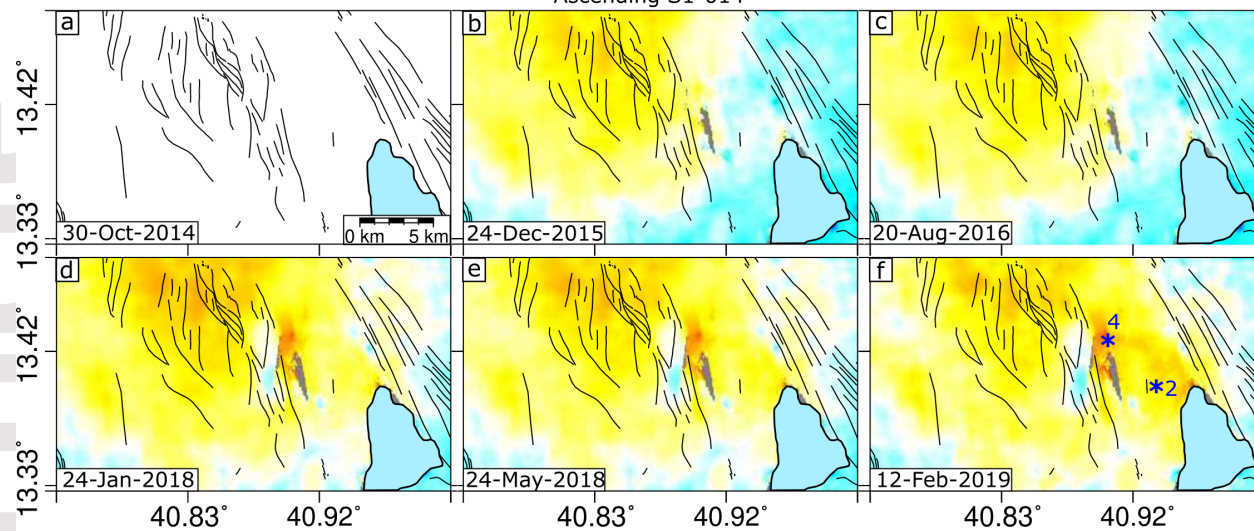
Descending ENV-049







Ascending S1-014



Descending S1-079

